

Quantitative analysis of two-component samples using in-line hard X-ray images

T. E. Gureyev,^{a*} A. W. Stevenson,^a D. M. Paganin,^{a,b}
T. Weitkamp,^c A. Snigirev,^c I. Snigireva^c and
S. W. Wilkins^a

^aCSIRO Manufacturing Science and Technology, PB 33, Clayton South, VIC 3169, Australia, ^bSchool of Physics, The University of Melbourne, VIC 3010, Australia, and ^cEuropean Synchrotron Radiation Facility, BP 220, 38043 Grenoble CEDEX, France.
E-mail: tim.gureyev@csiro.au

Methods for rapid quantitative phase-sensitive X-ray imaging of non-crystalline samples consisting of two distinct components are investigated. The transverse spatial distribution of the projected thickness of each component is reconstructed by computer processing of in-line images collected using synchrotron-generated hard X-rays and a position-sensitive detector with submicrometre spatial resolution. Different imaging techniques and associated image-processing algorithms are considered, with relative advantages and difficulties of each approach compared. A possible generalization of the method for the case of n -component samples is briefly discussed.

Keywords: hard X-rays; phase contrast; image analysis.

1. Introduction

In-line imaging using hard X-rays is an increasingly popular approach in rapid non-destructive analysis of non-crystalline samples. Among the attractive characteristics of this method are the availability of bright X-ray sources, relative simplicity of the experimental set-up and the ability to image the internal structure of optically opaque samples in their native state. Quantitative imaging with submicrometre spatial resolution has been demonstrated using synchrotron radiation (Gureyev *et al.*, 1999) and laboratory-based microfocus sources (Gureyev *et al.*, 2001). Useful applications have been found in material sciences, biology, medicine and many other areas.

It has been shown that in-line X-ray images of most samples usually combine conventional absorption contrast with phase contrast (Fitzgerald, 2000). The in-line phase contrast is due to the free-space propagation of the beam which transforms phase variations in the object plane into detectable intensity variations in the image plane, provided the propagation distance is large enough for the given imaging configuration and the sample. When the projection approximation is applicable to the propagation of X-rays through the sample, absorption contrast reflects the projected distribution of the imaginary part of the complex refractive index, while the near-field† phase contrast is proportional to the second derivatives of the projection of the real part of the refractive index (Wilkins *et al.*, 1996). Therefore, it should be possible to reconstruct the projected complex refractive index by means of appropriate analysis of in-line images. Simple considerations show that generally a single image is insufficient for such a reconstruction, as a two-dimensional complex distribution of the projected values of the refractive index would require at least two two-dimensional distributions of the (real-

† Note that in this paper we use the term ‘near-field’ for the region where the Fresnel number is much larger than one, *i.e.* $z \ll a^2/\lambda$, where z is the distance between the object and image planes, a is the size of the feature being imaged and λ is the wavelength.

valued) image-intensity data measured at the same number of points (pixels), but under different imaging conditions. Suitable image data can be collected, for example, at two or more different sample-to-detector distances, or at different X-ray wavelengths (Buckley *et al.*, 1997; Cloetens *et al.*, 1999; Gureyev *et al.*, 2001). Conventional tomographic methods can be used for the reconstruction of the three-dimensional distribution of both the real and imaginary components of the refractive index, if the projected distribution of the complex refractive index has been determined while illuminating the sample from multiple incident angles.

In this paper we study samples that can be regarded as consisting predominantly of two distinct materials (components) with known complex refractive indices. Practical examples may include biological samples containing bone as well as soft tissues, certain microelectronics components *etc.* The primary attractiveness of such samples for our study is in the relative simplicity of the corresponding theoretical model, due to which they can serve as a convenient stepping stone on the way to quantitative analysis of general n -component samples. We should also note that, owing to its specific structure, the sample that we used in this study could be analyzed by simpler alternative means, *e.g.* using only contact radiographs. However, we deliberately chose this simple and well characterized sample because our main goal here is to verify three recently proposed phase-retrieval methods which, if proven to be sufficiently accurate, can be applied to much more complex samples in the future.

2. Theory of phase and amplitude retrieval from near-field in-line images

Consider an object illuminated by a plane monochromatic wave with wavelength λ and unit intensity propagating along the optic axis z (Fig. 1). Under the projection approximation, the distributions of the logarithm of intensity, $M = \log I$, and the phase, φ , on the object plane, $z = 0$, can be expressed in terms of line integrals of the complex index of refraction, $n \equiv n(\mathbf{r}, \lambda) = 1 - \delta(\mathbf{r}, \lambda) - i\beta(\mathbf{r}, \lambda)$, $|n - 1| \ll 1$, $\mathbf{r} = (\mathbf{r}_\perp, z)$,

$$M(\mathbf{r}_\perp, 0, \lambda) = -(4\pi/\lambda) \int_{-t(\mathbf{r}_\perp)}^0 \beta(\mathbf{r}_\perp, z', \lambda) dz', \quad (1)$$

$$\varphi(\mathbf{r}_\perp, 0, \lambda) = -(2\pi/\lambda) \int_{-t(\mathbf{r}_\perp)}^0 \delta(\mathbf{r}_\perp, z', \lambda) dz', \quad (2)$$

where $t(\mathbf{r}_\perp)$ is the thickness of the sample. The dependencies of the real and imaginary parts of the complex refractive index on the wavelength of the incident radiation in the absence of absorption edges between λ_0 and λ for any elements present in the sample are well known (Arndt & Willis, 1966),

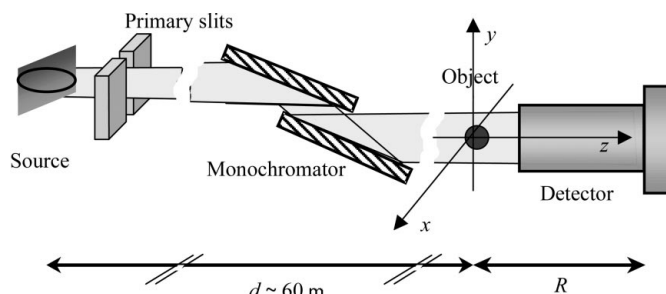


Figure 1
Imaging set-up.

$$\beta(\mathbf{r}, \lambda) = (\lambda/\lambda_0)^4 \beta(\mathbf{r}, \lambda_0), \quad (3)$$

$$\delta(\mathbf{r}, \lambda) = (\lambda/\lambda_0)^2 \delta(\mathbf{r}, \lambda_0). \quad (4)$$

It should be recognized that these equations are approximate and, in particular, may become less accurate at higher X-ray energies. In the near field, *i.e.* in the region where the Fresnel number is large, the free-space propagation of the beam from the object plane $z = 0$ to the image plane $z = R$ can be described using the ‘transport of intensity equation’ (TIE),

$$\gamma \nabla \cdot (I \nabla \varphi)(\mathbf{r}_\perp, 0, \lambda) = I(\mathbf{r}_\perp, R, \lambda) - I(\mathbf{r}_\perp, 0, \lambda), \quad (5)$$

where $\gamma = -R\lambda/(2\pi)$. This equation can be used for retrieving the object-plane phase distribution, if the intensity distributions over the object plane, $z = 0$, and over the image plane, $z = R$, are known (Teague, 1983). Any uniform boundary conditions can be used in conjunction with (5) if the sample is fully contained in the field of view.

Taking into account equations (1)–(4) and the fact that, in the region of validity of the TIE (in the near-field), $I(\mathbf{r}_\perp, R, \lambda)/I(\mathbf{r}_\perp, 0, \lambda) - 1 \cong \ln I(\mathbf{r}_\perp, R, \lambda) - \ln I(\mathbf{r}_\perp, 0, \lambda)$, we can rewrite the TIE equation (5) as

$$\sigma^3 M(\mathbf{r}_\perp, 0, \lambda_0) + \gamma \sigma (\nabla^2 \varphi)(\mathbf{r}_\perp, 0, \lambda_0) + \gamma \sigma^4 (\nabla \varphi \cdot \nabla M)(\mathbf{r}_\perp, 0, \lambda_0) = F, \quad (6)$$

where $\sigma = \lambda/\lambda_0$ and $F = \ln[I(\mathbf{r}_\perp, R, \lambda)]$. This form of the TIE explicitly takes into account the changes in the object plane intensity and phase with λ . If images at three different wavelengths λ_i , $i = 0, 1$ and 2 , are available, we can consider the following algebraic system of three linear equations,

$$A \begin{bmatrix} M(\mathbf{r}_\perp, 0, \lambda_0) \\ (\nabla^2 \varphi)(\mathbf{r}_\perp, 0, \lambda_0) \\ (\nabla M \cdot \nabla \varphi)(\mathbf{r}_\perp, 0, \lambda_0) \end{bmatrix} = \begin{pmatrix} F_0 \\ F_1 \\ F_2 \end{pmatrix}, \quad (7)$$

where

$$A = \begin{pmatrix} 1 & \gamma_0 & \gamma_0 \\ \sigma_1^3 & \sigma_1 \gamma_1 & \sigma_1^4 \gamma_1 \\ \sigma_2^3 & \sigma_2 \gamma_2 & \sigma_2^4 \gamma_2 \end{pmatrix},$$

and the right-hand side functions $F_i = \ln[I(\mathbf{r}_\perp, R, \lambda_i)]$ can be evaluated from the three measured intensity distributions in the image plane $z = R$ at the three selected wavelengths. It can be easily verified that the determinant of the matrix A cannot be equal to zero as long as all three wavelengths λ_i , $i = 0, 1, 2$, are different. Therefore, the logarithm of intensity and the Laplacian of the phase distribution in the object plane can be obtained as solutions to the linear system (7). The phase distribution can be retrieved by solving the Poisson equation,

$$-\nabla^2 \varphi(\mathbf{r}_\perp, 0, \lambda_0) = -\sum A_{ij}^{-1} F_j,$$

where A_{ij}^{-1} , $j = 0, 1$, and 2 , are the elements of the central row of the matrix inverse to A . A number of different numerical techniques based, for example, on the fast Fourier transform or multigrid methods can be used for numerical solution of the Poisson equation for the phase.

Let us consider an object consisting of only two materials with refractive indices $n_1(\lambda) = 1 - \delta_1(\lambda) - i\beta_1(\lambda)$ and $n_2(\lambda) = 1 - \delta_2(\lambda) - i\beta_2(\lambda)$. For such an object, (1) and (2) become

$$(-\lambda/4\pi)M(\mathbf{r}_\perp, 0, \lambda) = \beta_1(\lambda)T_1(\mathbf{r}_\perp, \lambda) + \beta_2(\lambda)T_2(\mathbf{r}_\perp, \lambda), \quad (8)$$

$$(-\lambda/2\pi)\varphi(\mathbf{r}_\perp, 0, \lambda) = \delta_1(\lambda)T_1(\mathbf{r}_\perp, \lambda) + \delta_2(\lambda)T_2(\mathbf{r}_\perp, \lambda), \quad (9)$$

where $T_i(\mathbf{r}_\perp, \lambda)$, $i = 1, 2$, are the projected thicknesses of the two materials. This system can be easily solved for T_1 and T_2 provided that $\Delta \equiv \beta_1 \delta_2 - \beta_2 \delta_1 \neq 0$,

$$T_1(\mathbf{r}_\perp, \lambda) = \lambda/(4\pi\Delta)[- \delta_2(\lambda)M(\mathbf{r}_\perp, 0, \lambda) + 2\beta_2(\lambda)\varphi(\mathbf{r}_\perp, 0, \lambda)], \quad (10)$$

$$T_2(\mathbf{r}_\perp, \lambda) = \lambda/(4\pi\Delta)[\delta_1(\lambda)M(\mathbf{r}_\perp, 0, \lambda) - 2\beta_1(\lambda)\varphi(\mathbf{r}_\perp, 0, \lambda)]. \quad (11)$$

We also consider an even simpler case of an object consisting of a single material with the refractive index $n(\lambda) = 1 - \delta(\lambda) - i\beta(\lambda)$ which does not depend on the position inside the sample. In this case the TIE can be rewritten as (Paganin *et al.*, 2001)

$$[1 + \gamma\delta/(2\beta)\nabla_\perp^2] \exp[-(4\pi/\lambda)\beta T(\mathbf{r}_\perp, \lambda)] = I(\mathbf{r}_\perp, R, \lambda). \quad (12)$$

A formal solution for the projected thickness $T(\mathbf{r}_\perp, \lambda)$ may be written on inspection,

$$T(\mathbf{r}_\perp, \lambda) = -\lambda/(4\pi\beta) \ln F^{-1}\{I(\mathbf{k}_\perp, R, \lambda)/[1 - \gamma\delta/(2\beta)\mathbf{k}_\perp^2]\}, \quad (13)$$

where F^{-1} denotes the inverse Fourier transform with respect to spatial frequencies \mathbf{k}_\perp dual to transverse spatial coordinates \mathbf{r}_\perp , and $I(\mathbf{k}_\perp, R, \lambda)$ is the Fourier transform of the image. Equation (13) can be efficiently evaluated using the fast Fourier transform and, hence, in this case the transverse spatial distribution of the sample thickness can be reconstructed from a single in-line image. The most important property of (13) is its high stability which is due to the filter $1/[1 - \gamma\delta/(2\beta)\mathbf{k}_\perp^2]$ being non-zero everywhere in the Fourier space (because $\gamma < 0$). This property can also be explained in terms of the underlying imaging physics (Paganin *et al.*, 2001). It may be important to note that, while the phase retrieval using the conventional TIE, equation (5), is independent from the analysis of the sample structure, the method utilizing equation (13) is based on an essential assumption about the sample, *i.e.* that the sample consists of a single material.

3. Experiment

A model sample was prepared by etching a simple relief in a polycarbonate substrate, and then filling the grooves with Cu. The one-dimensional relief, with 20 μm period, 10 μm -wide grooves of depth $\sim 2 \mu\text{m}$ and approximately rectangular profile of the grooves, was created in 0.5 mm \times 0.5 mm square regions of ~ 1 mm-thick polycarbonate plates by laser ablation. The grooves were then completely filled with Cu and a further flat layer of Cu was created on top of the structure by electroplating (see Fig. 2). The flatness of the resultant Cu surface was checked using an atomic force microscope.

The image data were gathered at the ID22 beamline of the European Synchrotron Radiation Facility. A quasi-plane monochromatic incident wave was prepared by consecutive reflection of the undulator beam first on a plane platinum-coated silicon vertical mirror and then a vertical double flat-crystal silicon 111 monochromator. Two rectangular pairs of slits, located upstream and downstream of mirror and monochromator (at 28 and 38 m from the source), were set to 1 mm \times 1 mm and 0.3 mm \times 0.3 mm, respectively.

The detector system for high-resolution microradiography at ID22 (Weitkamp *et al.*, 1999) consists of a single-crystal luminescent screen (Koch *et al.*, 1998), a visible-light microscope optic, and a FRLeLoN-2000 CCD camera (Labiche *et al.*, 1996) with 2048 by 2048 pixels to record the magnified image. For the present experiment, the scintillating screen was a 3.5 μm -thick lutetium aluminium garnet (LAG) (Koch *et al.*, 2000). The microscope was used with an overall magnification of 40, which resulted in an effective pixel size of 0.33 μm on the CCD. The linearity of the response signal as a function

of X-ray intensity incident on the detector was a characteristic particularly important for the quantitative analysis employed in the present work.

Images were collected at X-ray energies (wavelengths) $E = 17.2$ keV ($\lambda = 0.72$ Å), 20 keV ($\lambda = 0.62$ Å) and 23.8 keV ($\lambda = 0.52$ Å) at the sample-to-detector distances $R = 53, 83$ and 113 mm with the structured side of the sample towards the source. The exposure time was $t = 100$ s in all cases. At each X-ray energy E and each sample-to-detector distance R a flat-field image was also collected immediately after the corresponding image of the sample by translating the sample out of the beam and keeping other conditions constant. A dark-current image was collected with exposure $t = 100$ s and the X-ray shutter closed. The dark-current image and the flat-field images were used to correct the images of the sample in the standard fashion, *i.e.*

$$I_{\text{corrected}}(x, y; R, \lambda) = \frac{I_{\text{sample}}(x, y; R, \lambda) - I_{\text{dark}}(x, y)}{I_{\text{flat}}(x, y; R, \lambda) - I_{\text{dark}}(x, y)}. \quad (14)$$

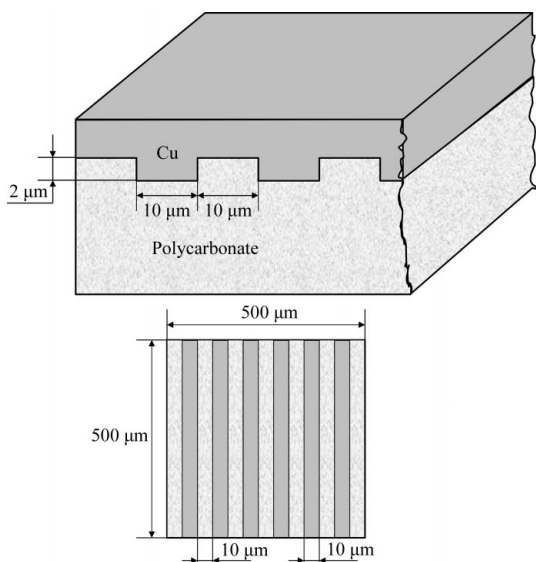


Figure 2
Schematics of the sample.

We used these corrected images collected at different sample-to-detector distances and with different X-ray wavelengths to reconstruct the spatial distribution of projected thickness of Cu and polycarbonate in the sample.

4. Processing of experimental images

We used the software package *XLI* developed in the X-ray Science and Instrumentation group of the CSIRO Manufacturing Science and Technology in Melbourne, Australia, for processing of the collected near-field in-line hard X-ray images as described by the theory presented in §2 above.

Images of our sample collected at $E = 17.2$ keV ($\lambda = 0.72$ Å) and at distances $R = 53, 83$ and 113 mm corrected for the detector dark current and flat field in accordance with (14) are presented in Figs. 3–5. The transverse (x - y) positions of the images were also correlated and corrected. Fig. 6 contains a vertical cross section through part of Fig. 4 showing typical phase-contrast effects at the

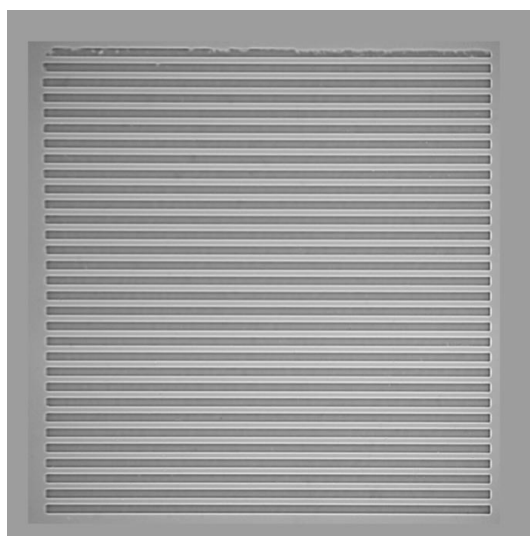


Figure 4
Image at $R = 83$ mm and $E = 17.2$ keV.

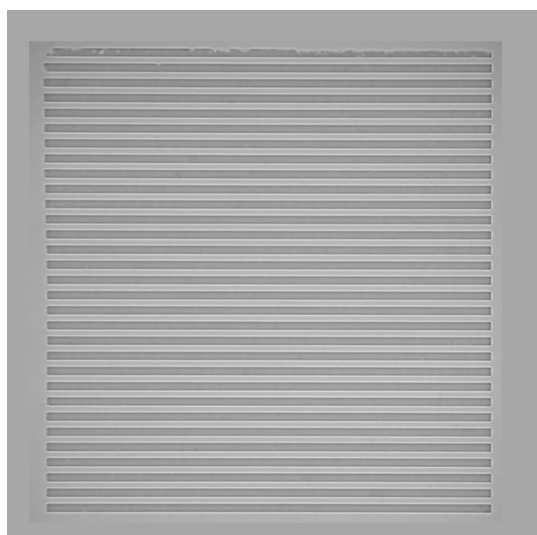


Figure 3
Image at $R = 53$ mm and $E = 17.2$ keV.

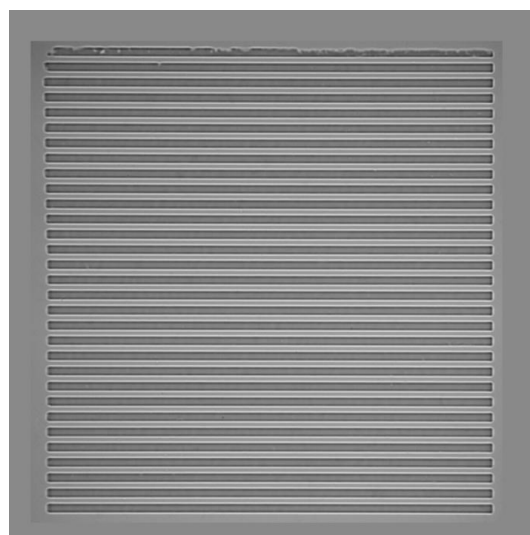


Figure 5
Image at $R = 113$ mm and $E = 17.2$ keV.

edges of the grooves. We used images Figs. 3–5 to solve (5) (with the left-hand side evaluated in the middle plane in order to increase the accuracy of the finite-difference approximation). The data from Figs. 3 and 5 were used to evaluate the right-hand side of equation (5), while the data from Fig. 4 were used for the intensity distribution on the left-hand side. We used the same uniform boundary conditions and multigrid algorithm to solve equation (5) as described previously elsewhere (see *e.g.* Gureyev *et al.*, 2001). We then calculated Kirchhoff integrals to simulate the propagation of the reconstructed complex amplitude from the plane $R = 83$ mm to the plane $R = 0$, and obtained the phase and amplitude distributions in the object plane. We then used (10) and (11) with the known values of δ and β for Cu and polycarbonate at $\lambda = 0.72$ Å, $\delta_{\text{Cu}} = 5.8 \times 10^{-6}$, $\beta_{\text{Cu}} = 2.7 \times 10^{-7}$, $\delta_{\text{PC}} = 8.9 \times 10^{-7}$ and $\beta_{\text{PC}} = 3.2 \times 10^{-10}$ to reconstruct the projected thicknesses of Cu and polycarbonate in the sample. The results are shown in Figs. 7 and 8, while Figs. 9 and 10 contain vertical cross sections through the reconstructed profiles. The maximum variation of the reconstructed projected thickness of both Cu and polycarbonate is relatively close to the expected value of 2 µm. However, the reconstructed profiles contain strong artifacts, most noticeable in the form of slow background variations in Fig. 8. Note that these background variations were much more pronounced in the original reconstructed profiles, and the results shown in Figs. 7 and 8 were obtained after the subtraction of background variations simulated with a low-pass Gaussian filter with a half-width $\sigma = 30$ µm. The artifacts are also more pronounced in the reconstructed profile of

polycarbonate (Figs. 8 and 10) compared with that of Cu. The reason for this is in the relatively larger contribution to the former of the reconstructed phase profile [see (10) and (11)], which contains more low-frequency artifacts. The origin of these low-frequency artifacts in the reconstructed phase distribution is in the residual background variations that can be seen in Figs. 3–5 on closer inspection, and that can be attributed primarily to the change of illumination (intensity distribution in the incident X-ray beam) between the exposures.

The sensitivity of the TIE-based phase retrieval in the near field to low-frequency noise in the image data is a well known phenomenon (Nugent *et al.*, 1996). Despite our best efforts to minimize the

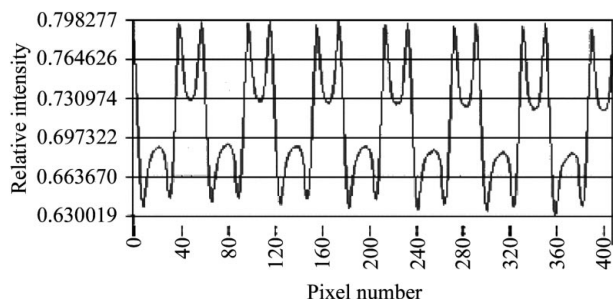


Figure 6
Vertical cross section through part of Fig. 4.

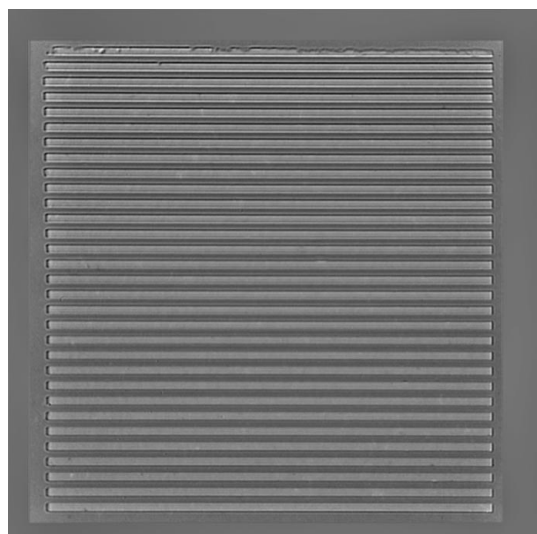


Figure 7
Distribution of projected thickness of Cu reconstructed from Figs. 3–5.

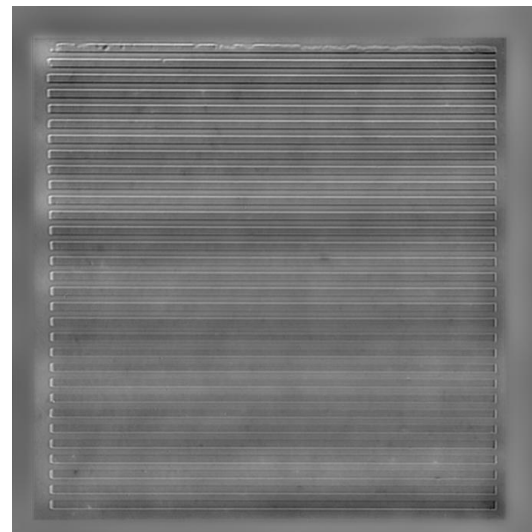


Figure 8
Distribution of projected thickness of polycarbonate reconstructed from Figs. 3–5.

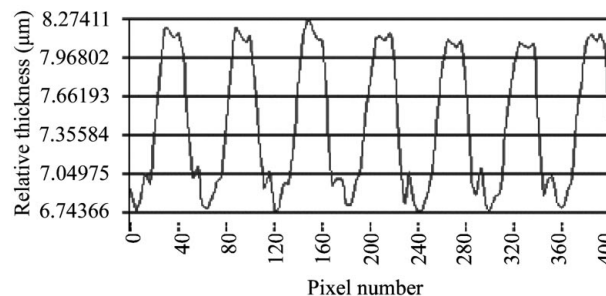


Figure 9
Vertical cross section through part of Fig. 7.

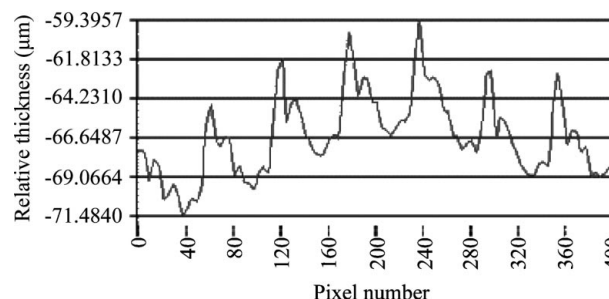


Figure 10
Vertical cross section through part of Fig. 8.

background variations between the exposures by collecting the images in quick succession, and attempts to minimize the oscillations in the incident beam, we have been unable to further reduce the background variation. As a result, the error in the reconstruction of projected thicknesses of the two components of the sample using images collected at different sample-to-detector distances was rather large as illustrated by Figs. 9 and 10

In the next experiment we collected images of the same sample at a fixed sample-to-detector distance $R = 53$ mm, but at three different X-ray energies (wavelengths) $E = 17.2$ keV ($\lambda = 0.72$ Å), 20 keV ($\lambda = 0.62$ Å) and 23.8 keV ($\lambda = 0.52$ Å) selected in quick succession by tuning the monochromator. The resultant images corrected for dark current and flat field had a visual appearance very similar to the images in Figs. 3–5. We then applied the algorithm corresponding to equations (7)–(11) to reconstruct the projected thickness of Cu and

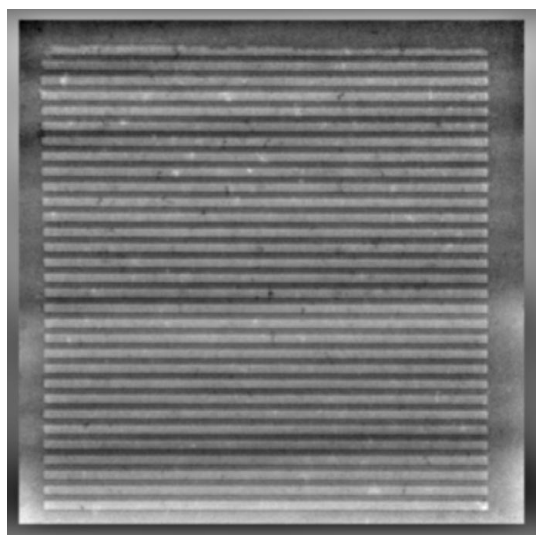


Figure 11
Distribution of projected thickness of Cu reconstructed from images collected at $E = 17.2$, 20 and 23.8 keV.

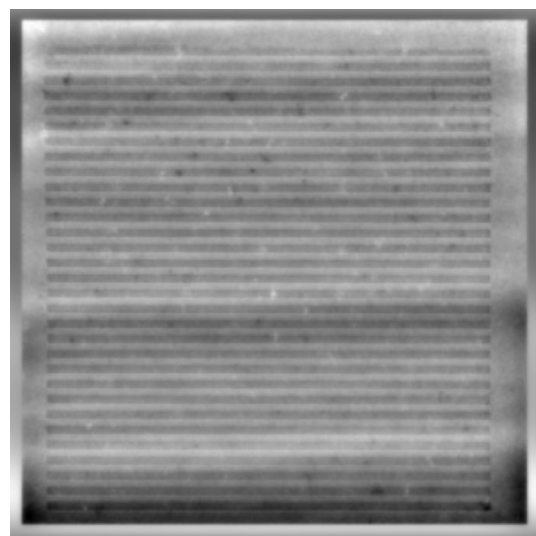


Figure 12
Distribution of projected thickness of polycarbonate reconstructed from images collected at $E = 17.2$, 20 and 23.8 keV.

polycarbonate from the three experimental images with the results shown in Figs. 11 and 12. In this case, the reconstructed thickness of polycarbonate was significantly different from the expected value of 2 μm . The errors in the reconstruction obtained using the multi-energy data are again attributable to the variations in the incident intensity distribution between the exposures.

Finally, we decided to use the special structure of our sample to utilize the reconstruction method described in equation (13). Indeed, although the latter method was developed for samples consisting of a single material (Paganin *et al.*, 2001), we could still apply it to our current sample, as the only transverse variation in the distribution of the projected complex refractive index corresponds to the *difference* between the refractive indices of Cu and polycarbonate: $\delta_{\text{Cu}} - \delta_{\text{PC}} = 4.91 \times 10^{-6}$ and $\beta_{\text{Cu}} - \beta_{\text{PC}} = 2.7 \times 10^{-7}$ at $\lambda = 0.72$ Å. Figs. 13, 14 and 15 show the results of application of the method based on equation (13) to experimental data from Fig. 3. Note that by the nature of this method the reconstructed profiles of Cu and polycarbonate are exactly complementary to each other. One can see that the reconstruction quality is quite high, while the values of the projected thickness of the relief (around 1.4 μm) are slightly smaller than the expected value of 2 μm . Application of this method to images obtained at other object-to-detector distances and with other X-ray energies produced similar results.



Figure 13
Distribution of projected thickness of Cu reconstructed from Fig. 3.

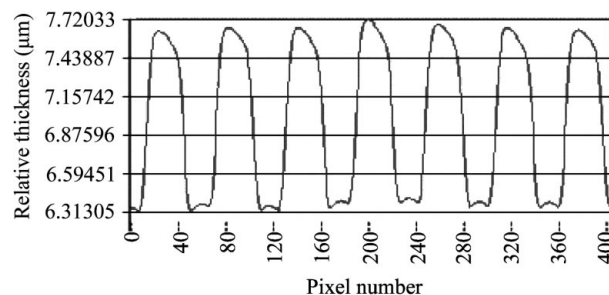


Figure 14
Vertical cross section through part of Fig. 13.

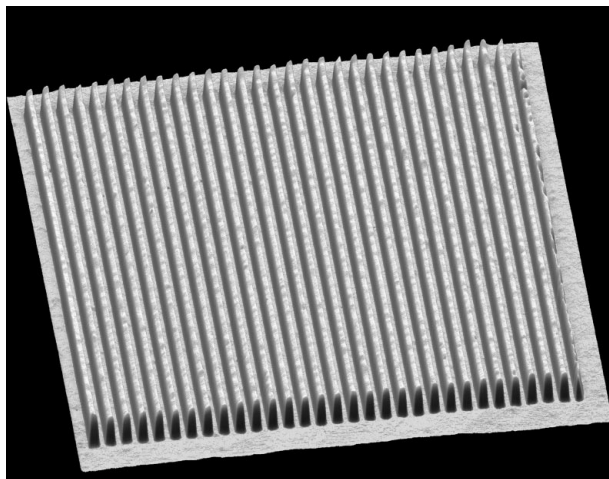


Figure 15
Three-dimensional representation of the distribution of projected thickness of Cu reconstructed from Fig. 3.

5. Conclusion

We have presented different methods for quantitative analysis of two-component samples using near-field in-line hard X-ray images. We have shown that the two-dimensional transverse spatial distribution of the thicknesses of the two components projected along the direction of the X-rays can be obtained from three images collected with the same X-ray wavelength but at different sample-to-detector distances, or at a fixed sample-to-detector distance, but with three different wavelengths.

Analysis of the experimental data collected at the ESRF synchrotron has demonstrated the importance of beam instabilities for this type of non-destructive analysis. In particular, it appears that, owing to the intrinsic insensitivity of the near-field in-line image contrast to low-frequency spatial variations of the object plane phase, the reconstruction is vulnerable to residual background oscillations in the incident intensity which may occur due to the beam instabilities. Such low-frequency background oscillations, which remained after the dark-current and flat-field corrections, have led to significant artifacts in the reconstructed distributions of phase and intensity in the object plane, that in turn translated into significant low-frequency errors in the reconstructed thicknesses of the sample components. We managed to obtain a good quality reconstruction using a method designed for objects consisting of a single material. For such objects, the phase and logarithm of intensity in the object plane are proportional to each other, and a single in-line image is sufficient for the reconstruction of the transverse spatial distribution of the object thickness. Although our sample consisted of two distinct materials (Cu and polycarbonate), the latter method was still applicable, because only the difference between the refractive indices of the two components influenced the image contrast due to the specific geometry of the sample. As this last method required only a single image for the reconstruction, it was unaffected by the variations of the incident intensity. It is also quite important that this method effectively utilizes absorption contrast at low frequencies, where the phase contrast is the weakest, thus avoiding the low-frequency instabilities which affect the other methods.

We would also like to briefly consider a generalization of these techniques to n -component samples. One can consider an analog of equations (8) and (9) with n , rather than two, terms on the right-hand side corresponding to n different materials. Obviously, to solve such a system one would generally need to know more than one set of phase and logarithm of intensity data in the left-hand side. Multiple sets of such data can be obtained at different X-ray wavelengths. However, it can be easily verified that due to (3) and (4) such generalization of (8) and (9) will be ill-conditioned (the system matrix will be degenerate). Therefore, in order to recover the projected thicknesses of each component in a sample consisting of more than two distinct materials, it is necessary to collect in-line images with X-ray wavelengths at different sides of absorption edges of some of the component materials. This technique is well known in conventional densitometry based on X-ray absorption. In some cases, however, phase contrast can be either preferable to absorption contrast (e.g. for hard X-rays and light elements) or simply unavoidable (e.g. in point-projection microscopy). In such cases the generalization of the techniques described in the present paper to n -component samples can be very useful for rapid quantitative X-ray analysis.

The authors acknowledge financial support provided by XRT Pty Ltd for this research. The experiment at the European Synchrotron Radiation Facility was carried out under the accepted proposal MI-413: 'Quantitative in-line holography with multi-energy hard X-rays' and was partially supported by a grant from the 'Access to Major Research Facilities Program' managed by the Australian Nuclear Science and Technology Organization. One of the authors (DMP) also acknowledges support from an Australian Research Council SPIRT grant. The authors are grateful to A/Professor E. Harvey, Dr J. Hayes and Dr B. Sexton for their help in sample preparation.

References

- Arndt, U. W. & Willis, B. T. M. (1966). *Single Crystal Diffractometry*, p. 185. Cambridge University Press.
- Buckley, C. J., Khaleque, N., Bellamy, S. J., Robins, M. & Zhang, X. (1997). *J. Phys. IV*, **7**(C2), 83–90.
- Cloetens, P., Ludwig, W., Baruchel, J., Van Dyck, D., Van Landuyt, J., Guigay, J.-P. & Schlenker, M. (1999). *Appl. Phys. Lett.* **75**, 2912–2914.
- Fitzgerald, R. (2000). *Phys. Today*, **53**, 23–26.
- Gureyev, T. E., Mayo, M., Wilkins, S. W., Paganin, D. & Stevenson, A. W. (2001). *Phys. Rev. Lett.* **86**, 5827–5830.
- Gureyev, T. E., Raven, C., Snigirev, A., Snigireva, I. & Wilkins, S. W. (1999). *J. Phys. D*, **32**, 563–567.
- Koch, A., Cloetens, P., Ludwig, W., Labiche, J.-C. & Ferrand, B. (2000). *Proceedings of the 5th International Conference on Inorganic Scintillators and their Applications (SCINT 99)*, pp. 157–166. Moscow: Lomonosov Moscow State University Press.
- Koch, A., Raven, C., Spanne, P. & Snigirev, A. (1998). *J. Opt. Soc. Am. A***15**, 1940–1951.
- Labiche, J.-C., Segura-Puchades, J., van Brussel, D. & Moy, J. (1996). *ESRF Newslett.* **25**, 41–43.
- Nugent, K. A., Gureyev, T. E., Cookson, D. F., Paganin, D. & Barnea, Z. (1996). *Phys. Rev. Lett.* **77**, 2961–2964.
- Paganin, D., Mayo, S. C., Gureyev, T. E., Miller, P. R. & Wilkins, S. W. (2001). *J. Microsc.* In the press.
- Teague, M. R. (1983). *J. Opt. Soc. Am.* **73**, 1434–1441.
- Weitkamp, T., Raven, C. & Snigirev, A. (1999). *Proc. SPIE*, **3772**, 311–317.
- Wilkins, S. W., Gureyev, T. E., Gao, D., Pogany, A. & Stevenson, A. W. (1996). *Nature (London)*, **384**, 335–338.